

Introduction of element Bi in the P-block promotes N₂ activation for efficient electrocatalytic nitrogen reduction to produce ammonia

Xiaoyue Chen ^a, Guangmin Ren ^a, Yaru Wang ^a, Zizhen Li ^a, Zisheng Zhang ^b, Xiangchao Meng ^{a,*}

^a Key Laboratory of Marine Chemistry Theory and Technology, Ministry of Education, College of Chemistry and Chemical Engineering, Ocean University of China, Qingdao 266100, China

^b Department of Chemical and Biological Engineering, Faculty of Engineering, University of Ottawa, Ottawa, Ontario K1N6N5, Canada



ARTICLE INFO

Keywords:
Electrocatalyst
Nitrogen reduction
P-block element
Bi₂S₃/MoS₂ composites

ABSTRACT

The synthesis of ammonia through electrocatalytic nitrogen reduction reaction (NRR) under ambient conditions is a presumable strategy. However, it still faces the problems of poor activity and low Faradic efficiency, so the development of efficient, stable and highly selective catalysts is of the importance. Molybdenum disulfide (MoS₂) materials are widely used in NRR reactions owing to good electrical conductivity and abundant active sites, but the edge active site is the dual active site of NRR and competitive hydrogen evolution reaction (HER). Encouragingly, the strong interaction between elements in the P-block and N 2p orbitals results in excellent performance in adsorbing and activating nitrogen. Meanwhile, the partial occupation of p-orbitals by elements in the P-block also leads to poor HER activity. Herein, we introduced the P-block element Bi into 1 T-MoS₂ and prepared Bi₂S₃/MoS₂ composite. Taking advantage of the high conductivity of 1 T-MoS₂ and the N₂ adsorption and activation advantages of Bi element, an ammonia yield rate of 54.64 µg h⁻¹ mg⁻¹cat. and a high Faradic efficiency of 58.56 % were obtained. In addition, the active site and the evolution pathway of N₂ reduction were investigated by in-situ infrared spectroscopy measurements and density functional theory (DFT). The in-situ infrared spectroscopy measurement results manifested the presence of the main intermediate transition state during the reduction of N₂ to NH₃. The calculation results indicated that N₂ had the best adsorption on the introduced P-block element Bi, and the entire NRR reaction process followed an alternating pathway. This study reveals the synergistic effect of P-block elements and transition metal-based electrocatalytic materials on nitrogen reduction to ammonia synthesis.

1. Introduction

Ammonia (NH₃) is not only plays an important role in the fertilizer industry and the storage of hydrogen, but also an industrial raw material for the production of nitrogen-containing compounds [1,2]. Currently, industrial ammonia production is the Haber-Bosch (H-B) process which was developed in 20th century [3]. The H-B process operated under critical conditions (300–500 °C, 20–40 MPa) with high energy consumption, vast amount of CO₂ emissions and low conversion rate (10–15 %) [4–8]. Developing a sustainable and green process that can utilize renewable resources to reduce N₂ to generate NH₃ under mild conditions has a major impact on agriculture, industrial development and energy reform in modern society. In recent years, electrocatalytic nitrogen reduction reaction (NRR) has been considered as one of the most promising alternative methods to the H-B process due to its ability

to be driven by renewable energy sources under environmental conditions (normal temperature and pressure, with H₂O as the proton source) [9]. Although it has many advantages, owing to the inherent chemical inertness and thermodynamic stability of nitrogen, which results in low ammonia yield rate and Faradic efficiency (FE), the severe challenges faced by electrocatalytic NRR mainly include: 1) extremely low solubility of N₂ in aqueous electrolytes, high dissociation energy of N≡N triple bond is high (945 kJ/mol), and difficulty in activating N₂[10]; 2) The theoretical reaction potential of NRR (0.09 V vs. RHE) is close to the potential of competitive HER, indicating a strong HER reaction [11,12].

Layered molybdenum disulfide (MoS₂) due to its two-dimensional layered structure and ability to form different crystal structures has received widespread attentions in the field of electrocatalytic NRR [13–15]. However, since the poor conductivity of the semiconductor phase 2 H-MoS₂ and active sites only exist at the lattice edges, the

* Corresponding author.

E-mail address: mengxiangchao@ouc.edu.cn (X. Meng).

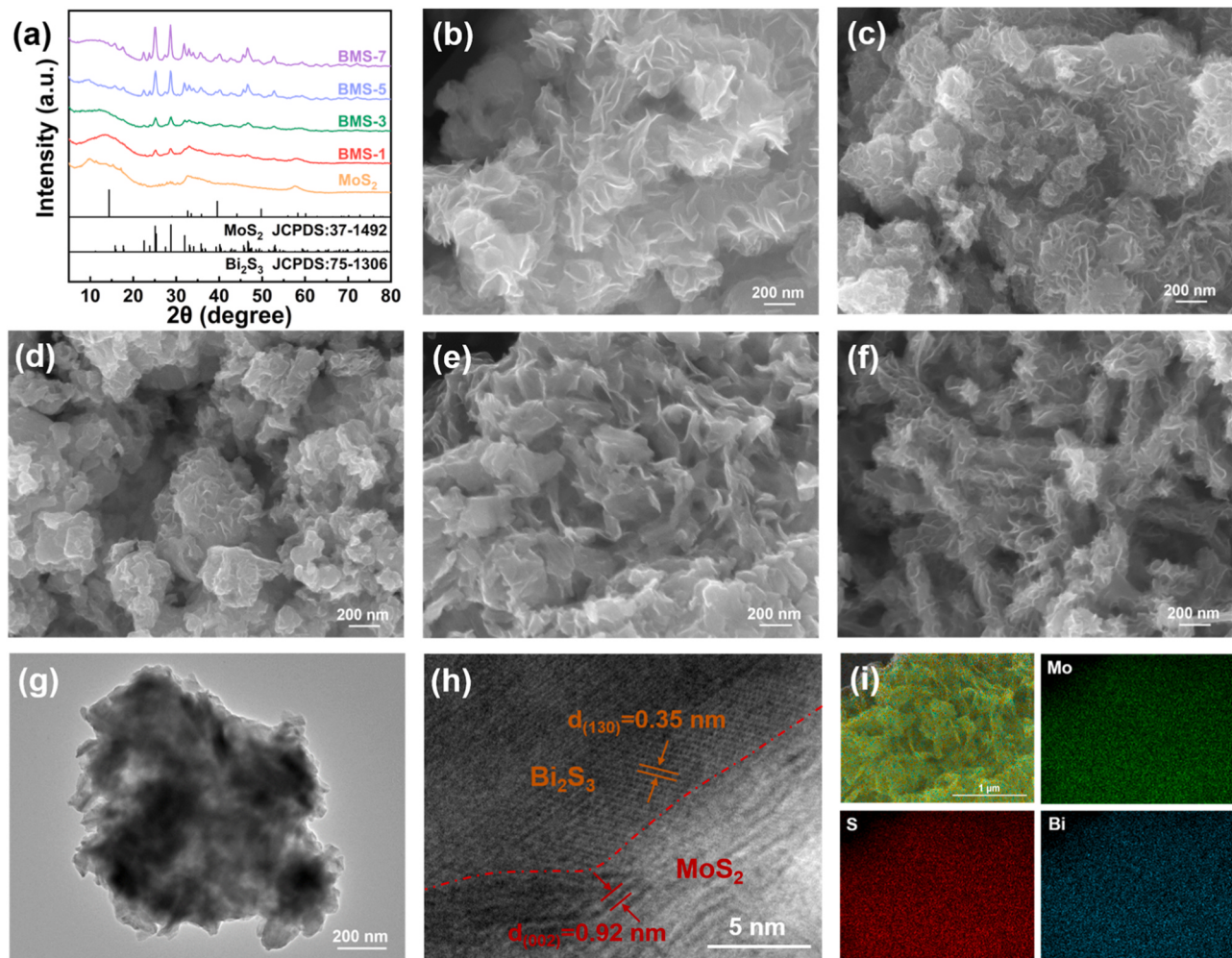


Fig. 1. (a) XRD patterns of MoS₂, BMS-1, BMS-3, BMS-5 and BMS-7; (b-f) SEM images of MoS₂, BMS-1, BMS-3, BMS-5 and BMS-7; (g) TEM image; (h) HRTEM image; (i) EDS images of BMS-5.

limited active sites caused by its inert basal plane severely limits its application prospects in NRR [13,16]. In contrast, the conductivity of the metallic phase 1 T-MoS₂ is much higher (~105 times) than that of the 2 H phase [17], and active sites exist on both its edges and basal surfaces, which makes it more attractive for NRR compared to 2 H-MoS₂ [16,18–20]. Notably, the edge sites of MoS₂ are active sites for both NRR and HER in electrocatalysis [21]. Suppressing the HER process may be further enhanced the electrocatalytic activity in NRR.

As reported, the P-block elements (e.g. B, Bi and In, et al.) and their compounds have been proven to have poor binding force with H-adatoms in competitive HER [22]. As one of the P-block elements, Bi with the unique extranuclear electron arrangement enables it to provide p electrons to the empty orbital of N₂ molecule, which is effective of activating N₂. Due to its poor ability to bond with H atoms and strong ability to donate p electrons, it results in poor HER performance [23,24]. Therefore, Bi based materials may be potential NRR electrocatalysts. Qiao's group [25] prepared two-dimensional bismuth nanosheets (Bi NS) by in-situ electrochemical reduction method for electrocatalytic N₂ reduction. As for the fully exposed edge active sites and effective p-orbital electron delocalization in Bi NS, the ammonia yield rate reached 13.23 $\mu\text{g h}^{-1} \text{mg}_{\text{cat}}^{-1}$, and the Faradic efficiency was improved to 10.46 %. Chu's group [26] reported on sulfur-deficient Bi₂S_{3-x} coupled Ti₃C₂T_x-Mxene (Bi₂S_{3-x}/Ti₃C₂T_x), obtained the ammonia yield rate of 68.3 $\mu\text{g h}^{-1} \text{mg}^{-1}$ and FE of 22.5 %. The excellent NRR activity was mainly due to the synergistic effect of the dual active sites, the S-vacancy and the interfacial Bi-site promoted the adsorption of N₂ and the first

hydrogenation to *NNH. Overall, the advantages of P-block elements can be concluded as: 1) The empty p orbitals can accept the lone pair of electrons of N₂ molecule, while the strong interaction between occupied p orbitals and N 2p orbitals can transfer electrons to the π^* orbitals of N₂ through "π-backdonation", which greatly weakens the stability of the N≡N triple bond; 2) The unique crystal structure and adjustable band gap enable the P-block metal-based electrocatalyst to be modified reasonably; 3) The p orbitals partially occupied by P-block elements inhibit the adsorption of H⁺ and inhibit the occurrence of HER to a certain extent [27,28].

In this work, we tried to combine the P-block element Bi with MoS₂ by one-step hydrothermal method, where the strong interaction between P-block element Bi and N 2p orbitals is beneficial to the adsorption and activation of N₂. The morphology and structure of the prepared catalyst were characterized, and its NRR performance was tested in 0.1 M Na₂SO₄. Furthermore, in-situ infrared spectroscopy testing and DFT calculations were executed to verify the N₂ reduction evolutionary pathway of Bi₂S₃/MoS₂ composites. Both experimental and theoretical calculation results had demonstrated that the prepared Bi₂S₃/MoS₂ composites exhibited excellent NRR performance.

2. Experimental section

2.1. Chemicals

Thiourea (CH₄N₂S, AR), Salicylic acid (C₇H₆O₃, AR), Sodium

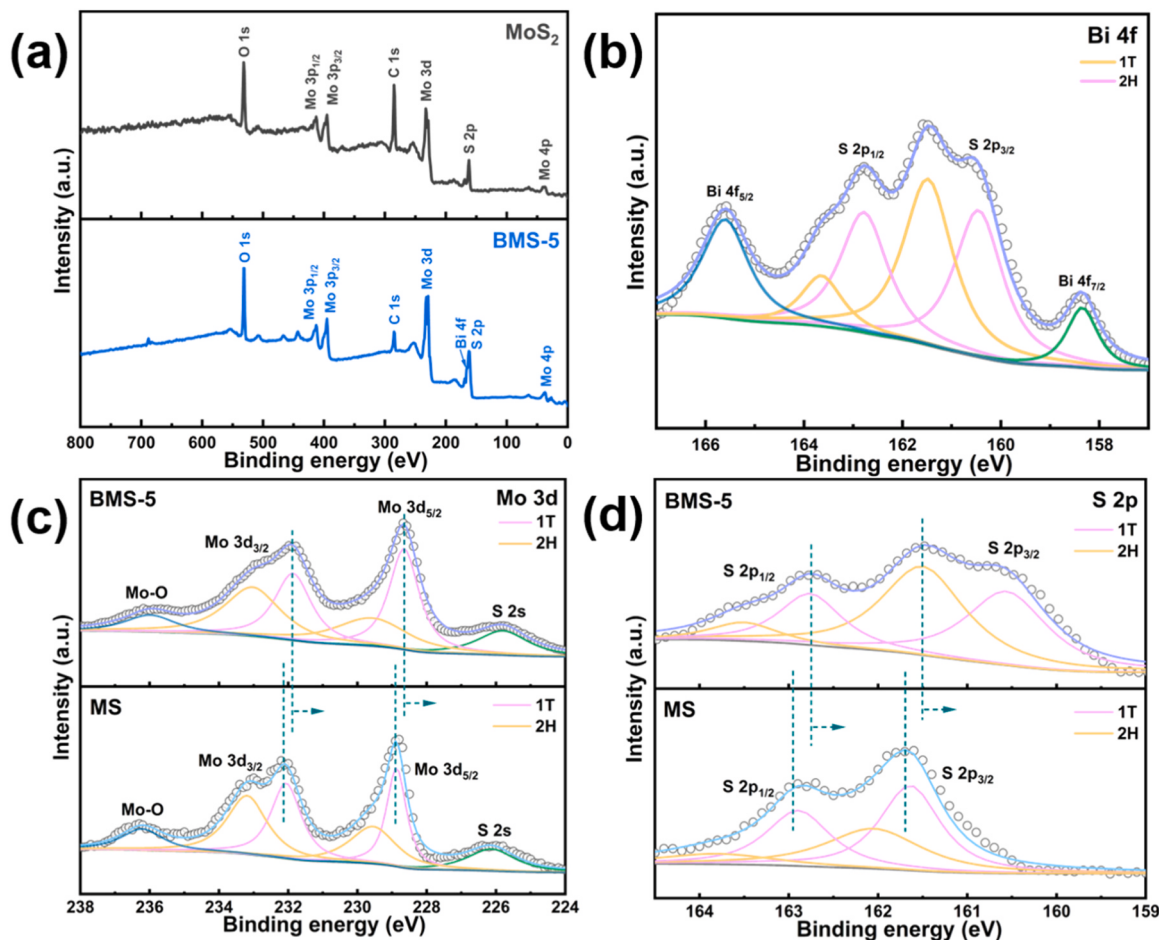


Fig. 2. (a) Survey spectrum of pure MoS_2 and BMS-5 composites; (b-d) XPS spectra of BMS-5 composites for Bi 4f, Mo 3d and S 2p, respectively.

hydroxide (NaOH, AR) and Bismuth nitrate pentahydrate ($\text{Bi}(\text{NO}_3)_3 \cdot 5 \text{H}_2\text{O}$) were purchased from Sinopharm Chemical Reagent Co., Ltd. Sodium hypochlorite solution (NaClO, AR), Ammonium molybdate tetrahydrate ($(\text{NH}_4)_6\text{Mo}_7\text{O}_{24} \cdot 4\text{H}_2\text{O}$, AR) and Sodium nitroferricyanide (III) dihydrate ($\text{Na}_2[\text{Fe}(\text{NO})(\text{CN})_5] \cdot 2\text{H}_2\text{O}$, AR) were provided by Shanghai Aladdin Biochemical Technology Co., Ltd.

2.2. Synthesis of pure MoS_2 and $\text{Bi}_2\text{S}_3/\text{MoS}_2$

Firstly, 1.16 g of $(\text{NH}_4)_6\text{Mo}_7\text{O}_{24} \cdot 4\text{H}_2\text{O}$, 1.06 g of $\text{CH}_4\text{N}_2\text{S}$ and 0.17 g of $\text{Bi}(\text{NO}_3)_3 \cdot 5 \text{H}_2\text{O}$ were dissolved in 70 mL of deionized water with ultrasonic treatment. The precursor solution was transferred into 100 mL Teflon-lined stainless-steel autoclaves (Anhui Kemi Instrument Co., Ltd, China) and maintained at 180 °C for 12 h in an oven. The composites obtained was named as BMS-5. The addition amounts of $\text{Bi}(\text{NO}_3)_3 \cdot 5 \text{H}_2\text{O}$ were changed to 0.0340 g, 0.1019 g and 0.2377 g, to obtain composites with different Bi addition amounts, named as BMS-1, BMS-3 and BMS-7, respectively. For comparison, pure MoS_2 was prepared using the same hydrothermal method without the addition of $\text{Bi}(\text{NO}_3)_3 \cdot 5 \text{H}_2\text{O}$.

3. Results and discussion

The XRD patterns of as-prepared samples were shown in Fig. 1a, which could be matched with MoS_2 (JCPDS No: 37-1492) and Bi_2S_3 (JCPDS No: 75-1306). The diffraction peak at 9.8° corresponded to the (002) plane of MoS_2 [29,30], which was the c-plane of MoS_2 formed by the coordination of Mo atoms and S atoms to form the S-Mo-S intermediate layer[31,32]. The six strong diffraction peaks at 25.29°, 28.73°,

31.92°, 35.75°, 46.80° and 52.91° could be attributed to the (130), (230), (221), (240), (501) and (351) crystal planes of Bi_2S_3 [33,34]. The XRD patterns of the composite material included both the diffraction peaks of Bi_2S_3 and MoS_2 , indicating that the $\text{Bi}_2\text{S}_3/\text{MoS}_2$ composites were synthesized without changing the crystal phase, and the characteristic peaks of Bi_2S_3 became more pronounced with the increase of Bi addition. In order to further obtain the surface morphology of the catalyst, the synthesized $\text{Bi}_2\text{S}_3/\text{MoS}_2$ composites were characterized by SEM (Fig. 1b-f). Fig. 1b showed the SEM image of pure MoS_2 , displaying the typical nanosheet flower structure. The SEM morphology of the composites with Bi added were shown in Fig. 1c-f. As the Bi content increases, the morphology of MoS_2 nanoflowers gradually transformed into a layered structure, and at the maximum Bi content, a rod-shaped structure was formed due to the presence of Bi_2S_3 (Fig. 1f). Similarly, as shown in Fig. 1g, the same sheet-like structure was observed in TEM images. The crystal faces of MoS_2 (002) and Bi_2S_3 (130) could be observed simultaneously in HRTEM images, with lattice fringe spacing of 0.92 nm and 0.35 nm, respectively (Fig. 1h)[35-37]. In addition, the clear interface indicated coupling between ordered crystals of MoS_2 and Bi_2S_3 . The EDS element mapping images showed the Mo, S, and Bi atoms were well-distributed in $\text{Bi}_2\text{S}_3/\text{MoS}_2$ electrocatalysts, indicating the successful introduction of Bi (Fig. 1i).

XPS characterization is aimed at further studying the elemental composition and corresponding chemical valence states of the prepared materials (Fig. 2a-d). Fig. 2a showed the XPS survey of original MoS_2 and $\text{Bi}_2\text{S}_3/\text{MoS}_2$ composites, with peaks consistent with the required elements, including Mo, S, and Bi (it is worth noting that C element was used for calibration, while O element might originate from surface oxidation)[38]. The Bi 4f spectrum in Fig. 2b exhibited strong peaks at

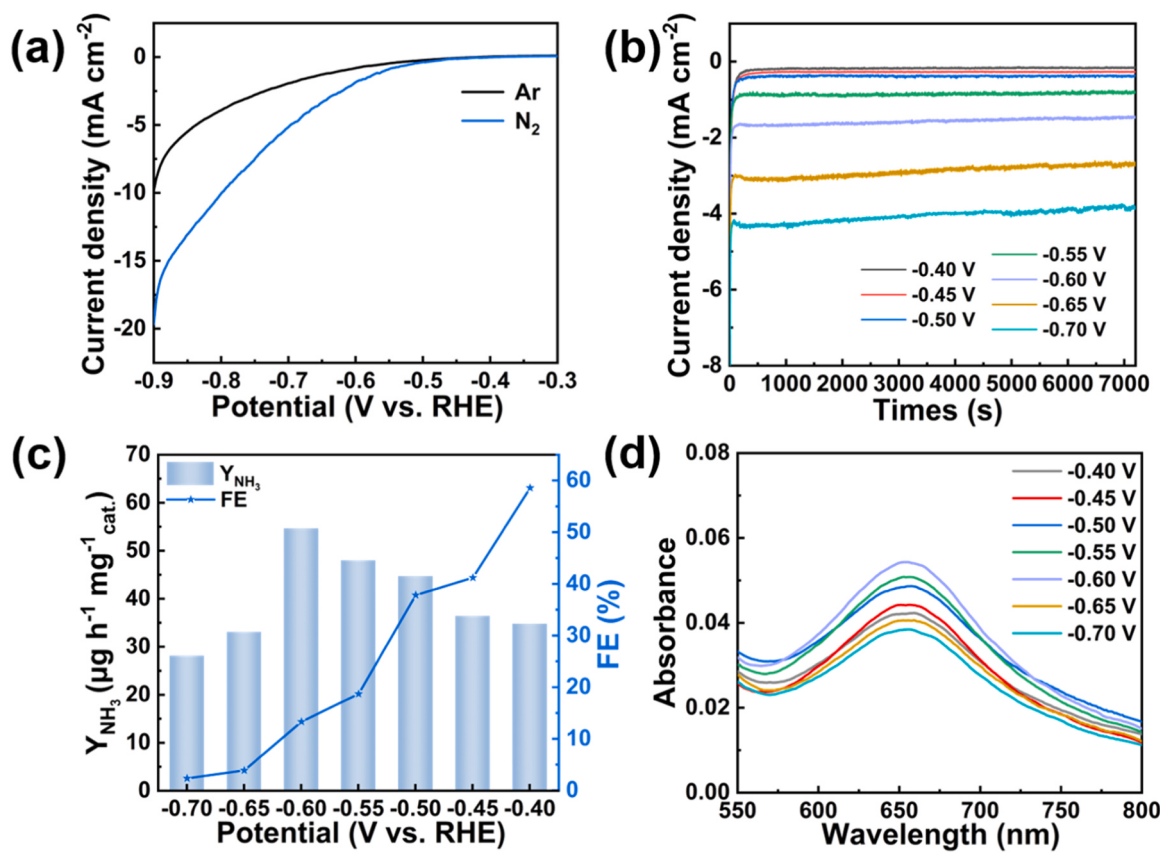


Fig. 3. (a) LSV curves recorded in Ar-saturated (black line) and N₂-saturated (blue line) 0.1 M Na₂SO₄; (b) Time-dependent current density curves at different potentials; (c) NH₃ yield rates and FE of BMS-5 at each potential; (d) UV-Vis absorption spectra (voltage vs. RHE).

the binding energies of 165.60 eV and 158.34 eV, respectively attributed to Bi 4 f_{5/2} and Bi 4 f_{7/2} for Bi (III)[27,39]. At the same time, S 2p peaks could be observed between the two peaks of Bi[40]. The peaks at 231.86 eV and 228.65 eV were observed in the Mo 3d spectrum to move about 0.9 eV towards the lower binding energy compared to Mo⁴⁺ 3d_{3/2} and Mo⁴⁺ 3d_{5/2} of 2 H-MoS₂, confirming the existence of the metal 1 T phase[41]. The Mo-O peak at 235.98 eV was due to the unavoidable surface oxidation of MoS₂ in the air. (Fig. 2c)[34,37] For the S 2p spectrum in Fig. 2d, the double peaks at 163.50 eV and 161.50 eV correspond to S 2p_{1/2} and S 2p_{3/2} and are attributed to 2 H phase MoS₂. In addition to the known 2 H phase double peaks, there were additional double peaks at 162.76 eV and 161.50 eV, further demonstrating the existence of the 1 T phase[42–44]. Notably, the Mo 3d and S 2p spectra (Figs. 2c and 2d) in Bi₂S₃/MoS₂ composites shifted negatively towards low binding energy compared to pure MoS₂, and the electron cloud density on the MoS₂ side increased, resulting in local electron-rich regions on the surface. The change in binding energy in Bi₂S₃/MoS₂ composites indicated the existence of electronic interaction between Bi₂S₃ and MoS₂, which was beneficial to promote effective electron transfer during the N₂ reduction process and increase the reaction rate. According to the above results, the successful synthesis of Bi₂S₃/MoS₂ composite materials was further confirmed.

In order to investigate the NRR performance of BMS-5, electrochemical nitrogen reduction reaction measurements were conducted in an H-type electrolytic cell separated by Nafion 117 membrane for proton exchange. In order to avoid NH₃ or NO_x pollution contained in the introduced N₂, the absorbance curves of NH₃, NO₃⁻ and NO₂⁻ in the 0.1 M Na₂SO₄ electrolyte before and after 30 minutes of N₂ bubbling after purification were respectively tested. As can be seen from Figure S1–S3, the absorbance of the gas did not change significantly before and after passing into the electrolyte, indicating that the purified gas did not

contain NH₃ or NO_x.

In order to test the nitrogen reduction performance of BMS-5, linear scanning voltammetry (LSV) curves were obtained in electrolyte solutions in Ar and N₂ atmospheres, respectively. In the potential range of $-0.40 \text{ V} \sim -0.90 \text{ V}$ vs. RHE, BMS-5 obtained a higher current density in N₂ atmosphere than in Ar atmosphere, which meant that the prepared catalyst exhibited N₂ reduction activity within this potential range (Fig. 3a). Besides, compared to pure MoS₂, BMS-5 exhibits poorer HER performance in Ar-saturated electrolytes, suggesting that the prepared composite structure catalyst could obviously inhibit the hydrogen evolution activity of MoS₂ (Figure S4). As shown in Fig. 3b, the NRR catalytic activity of BMS-5 was characterized by the chronoamperometric curve. The results showed that the prepared catalyst BMS-5 could maintain stable under different potentials without a significant decrease in current density. NH₃ yield rates and FE under different potentials were calculated, as shown in Fig. 3c. The ammonia yield rates of BMS-5 increased with the increase of potential, reaching a maximum of 54.64 $\mu\text{g h}^{-1} \text{ mg}_{\text{cat}}^{-1}$ at -0.60 V vs. RHE, while the maximum of Faradic efficiency reached 58.56 % at -0.40 V vs. RHE. As the potential continued to become negative, the NH₃ yield rates and FE of BMS-5 decreased, indicating that HER dominated[45]. The corresponding UV-Vis absorbance curve was shown in Fig. 3d. Furthermore, the absorbance curve of the blank bare electrode after electrolysis for 2 h was also tested, but the NH₃ yield was not detected, indicating that the catalyst was indispensable in the NRR process (Figure S5a). The current density curve shown in Figure S5b identified a significant increase in current density in the presence of catalyst BMS-5, indicating the occurrence of nitrogen reduction reaction.

Chronoamperometric curve were carried out in electrolyte solutions saturated with Ar and N₂ respectively, and it was clearly perceived that the current density in N₂ was significantly more negative than that in Ar,

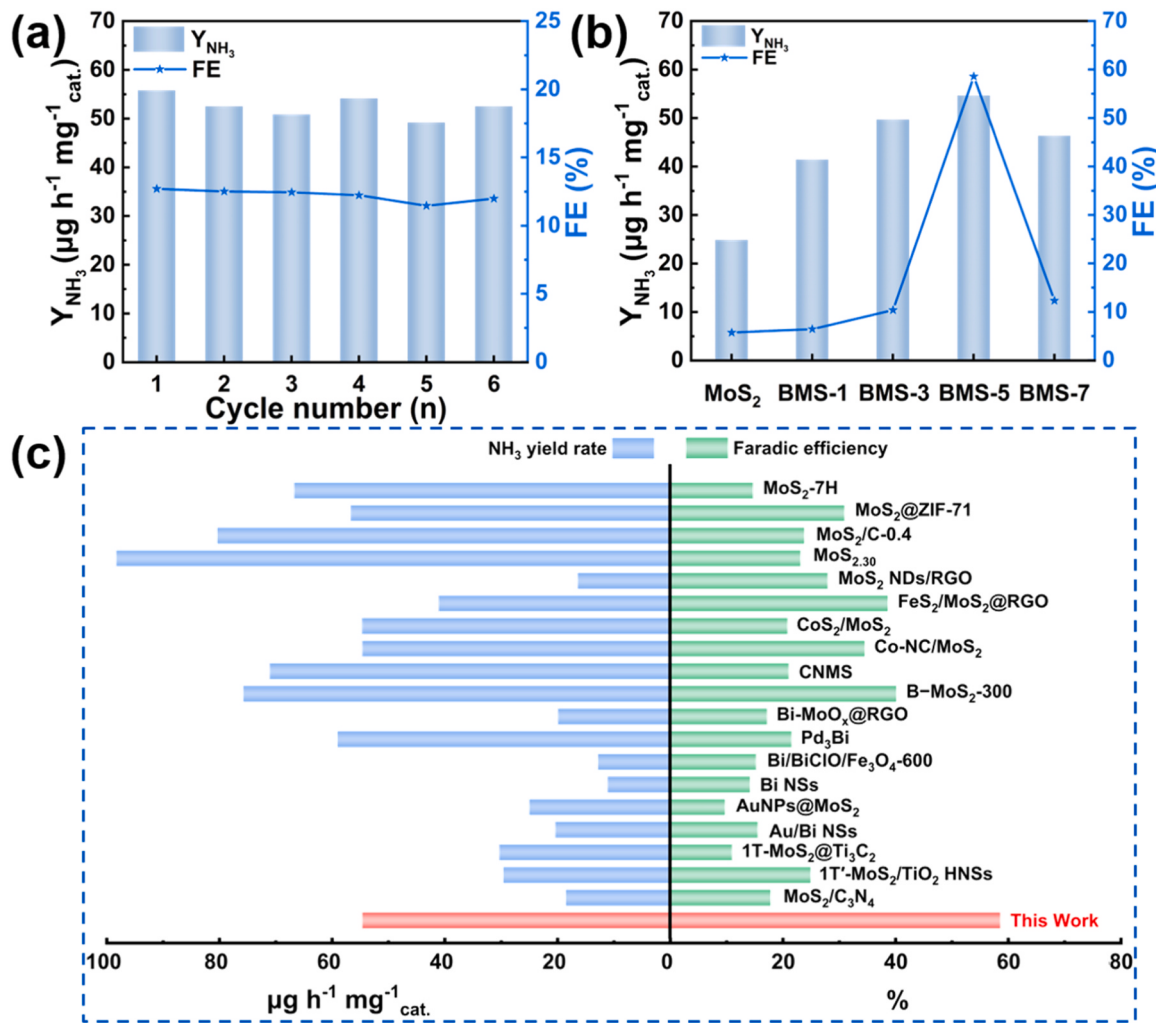


Fig. 4. NH₃ yield rates and FEs: (a) BMS-5 at -0.60 V vs. RHE during recycling tests; (b) Bi₂S₃/MoS₂ composites with different Bi content; (c) Comparison of the NRR performance of BMS-5 and other catalysts at ambient condition.

and the results showed that NRR reaction occurred in N₂. In addition, the presence of ammonia was not detected in the Ar atmosphere, further proclaiming that NH₃ was generated by electrocatalytic reduction of BMS-5 in nitrogen atmosphere (Figure S6). Additionally, as shown in Figure S7, chronoamperometric curve were tested at the open circuit potential (OCP) and -0.60 V vs. RHE in N₂ atmosphere, showing an obvious current density difference, and the absorbance curve showed that no ammonia was detected at the OCP, indicating that the applied voltage was a necessary condition for the NRR reaction.

The stability of catalyst was an important indicator to evaluate its performance. Five cycle tests were performed without replacing the working electrode, and the corresponding UV-Vis absorbance curves were shown in Figure S8a. Within the recycling tests, there was no significant decrease in NH₃ yield rates and FEs, indicating that BMS-5 had good stability (Fig. 4a). Besides, as shown in Figure S8b, the time-dependent current density curves remained stable during the recycling tests. The current density also did not show a downward trend during the long-term electrolytic test at 12 h, further demonstrating the excellent stability of BMS-5 catalyst (Figure S9). The most common by-product N₂H₄ in the NRR process was detected, and Figure S10 displayed that the presence of N₂H₄ was not detected before and after the experiment, indicating that BMS-5 had high selectivity for N₂ electro-reduction to synthesize NH₃. Furthermore, as the Bi content increased, the NH₃ yield rates and Faradic efficiency continued to increase, and BMS-5 showed the highest NH₃ yield rate of $54.64 \mu\text{g h}^{-1} \text{mg}^{-1}_{cat.}$ and the

highest FE of 58.56 % (Fig. 4b). However, when the Bi content was further increased, its NRR performance was decreased, possibly because excessive Bi was not conducive to the adsorption of H⁺ protons on the catalyst surface. The corresponding electrical impedance spectroscopy (EIS) measurement results (Figure S11) showed that after constructing the heterointerface, as-prepared Bi₂S₃/MoS₂ composites had a smallest Nyquist plots and lowest charge transfer resistance among the electrocatalysts, which may be due to the accelerated electron transfer speed after the construction of the heterointerface and the electrocatalytic NRR kinetics was enhanced. We compared the morphology, chemical composition, and elemental valence states of the catalysts after the reaction. As shown in Figure S12, the morphology was negligibly influenced during the NRR test. Moreover, XPS analysis showed that there was negligible change in the chemical composition and elemental valence states of the composites after the NRR test (Figure S13). These results confirmed that as-prepared electrocatalyst exhibited high chemical stability when applied in electrocatalytic reduction of N₂ to produce ammonia. Meanwhile the NRR performance of other Bi based and Mo based electrocatalytic materials was compared (Fig. 4c and Table S1), and the prepared BMS-5 exhibited excellent activity.

For further clarify the reaction pathway of Bi₂S₃/MoS₂ composites converting nitrogen to ammonia, in situ infrared spectroscopic measurements were conducted (Fig. 5a). For BMS-5, the absorption peak at $\sim 1650 \text{ cm}^{-1}$ could be owed to chemisorbed N₂, indicating that the catalyst had good adsorption ability for dissolved N₂ in the electrolyte

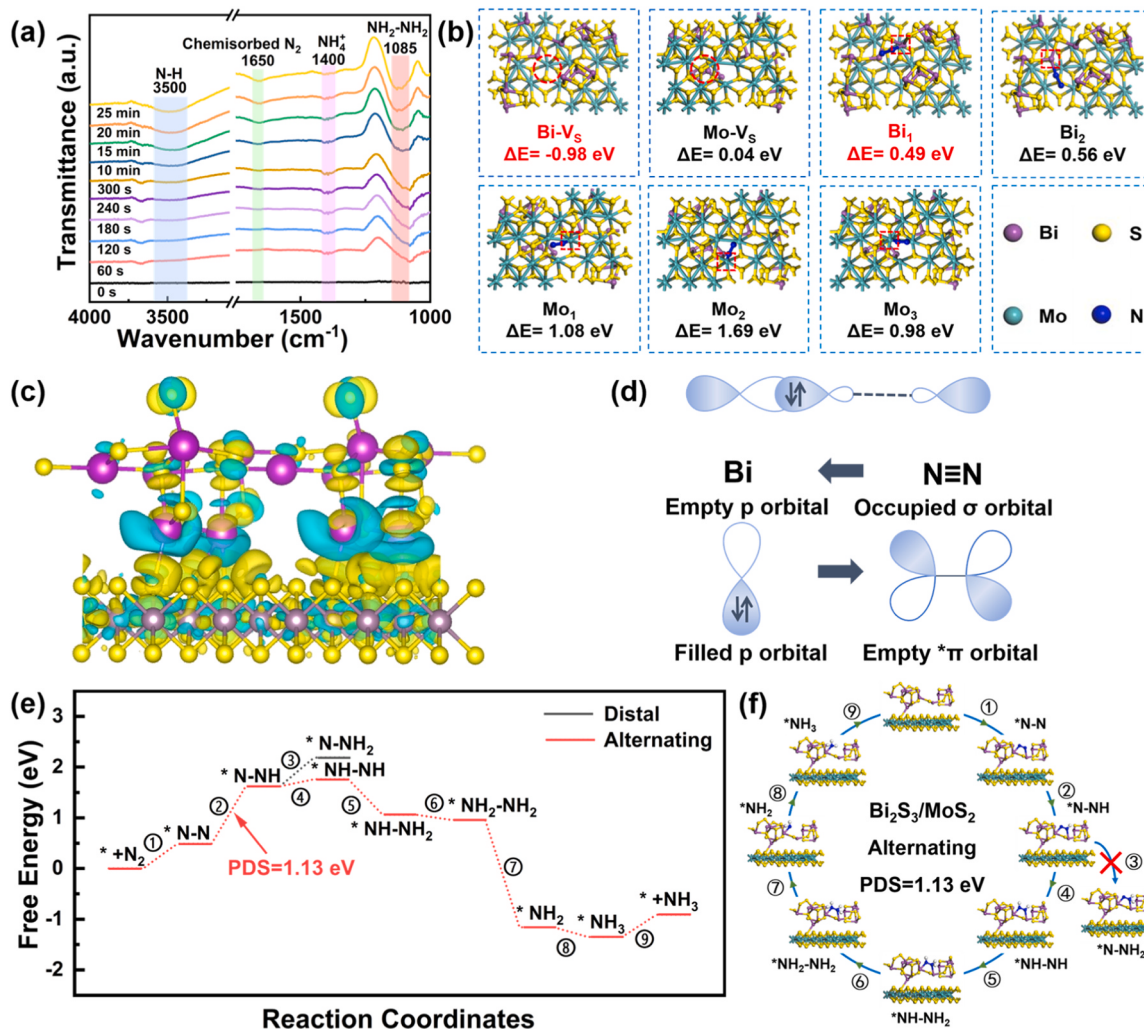


Fig. 5. (a) In situ infrared spectra of BMS-5 at -0.60 V vs. RHE; (b) The vacancy formation energy of S vacancies at different sites and the adsorption energy of N₂ on different Bi/Mo sites near the S vacancy; (c) Charge density difference of Bi₂S₃/MoS₂ composites; (d) Simplified schematic diagram of N₂ bonding to Bi; (e) Gibbs free energy diagrams for NRR on Bi₂S₃/MoS₂ composites through distal pathway (black line) and alternating pathway (red line); (f) Schematic diagram of ammonia synthesis by using Bi₂S₃/MoS₂ composites.

solution [46]. In addition, the characteristic absorption peaks at ~ 3500 and ~ 1085 cm⁻¹ belonged to N-H and NH₂-NH₂ [47,48], respectively, which were transition states in the NRR reaction process, and the absorption intensity of these characteristic peaks increases with the progress of the reaction. The peak at ~ 1400 cm⁻¹ was characteristic peak of NH₄⁺, further confirming the generation of NH₄⁺ during the experimental process. In an effort to more clearly elucidate the mechanism of N₂ reduction to NH₃ on Bi₂S₃/MoS₂ composites, theoretical DFT calculations were performed to determine the optimal adsorption sites and evolutionary paths of N₂ molecules. Firstly, the energy required to form an S-vacancy on the surface of Bi₂S₃ and MoS₂ was calculated respectively, as shown in Fig. 5b. The results manifested that vacancy was more likely to form on the surface of Bi₂S₃ ($\Delta E = -0.98$ eV), so the calculation of the subsequent NRR reaction process was based on the above results. Subsequently, the adsorption energy of N₂ on different Bi/Mo sites near the S vacancy was calculated (Fig. 5b). From the results obtained so far, the energy required for N₂ to adsorb on Bi₁ sites ($\Delta E = 0.49$ eV) was much lower than that required for N₂ to adsorb on Mo sites, mainly because Bi could interact with N₂ through p- π interactions [49]. Fig. 5c exhibited charge density difference of Bi₂S₃/MoS₂ composites. It could observe obvious electron agglomeration at the interface, and a local poor electronic area was formed on the Bi₂S₃ side, which could accommodate lone pair electrons of N₂ molecules, consistent with

XPS results. In addition, N₂ molecules belonged to Lewis bases, and the S vacancies formed were anionic vacancies, presenting an electron deficient state, which was conducive to the adsorption of nitrogen on metal atoms around the vacancies, further creating favorable conditions for the stable adsorption of N₂ on Bi. Meanwhile, the bonding of Lewis acid H⁺ at the electron-deficient site was also inhibited, thus increasing the FE of NRR [45]. These results indicated that the Bi₂S₃/MoS₂ composites interface exhibited electron enrichment, and N₂ adsorbed in the locally electrophilic Bi₂S₃ region could be further activated by an energy-first side-on configuration. Notably, the activation of N₂ molecules needed to follow the previously reported "donation-backdonation" process [23, 50]. The empty orbital of Bi firstly accepted electrons from the occupied σ orbital of N₂ molecule (σ -donation), and the occupied orbital of Bi assigned electrons to the empty π^* orbital of N₂ molecule (π -backdonation), thus realizing the effective activation of N₂ molecule on the surface of the electrocatalyst (Fig. 5d). As shown in Figs. 5e and 5f, after structural optimization, N₂ tended to adsorb on the two Bi atoms adjacent to the S vacancy through bridging adsorption. Then, the Gibbs free energies (ΔG) of the distal and alternating pathways of N₂ hydrogenation evolution on the surface of Bi₂S₃/MoS₂ composites were calculated. The first step of hydrogenation (*NN \rightarrow *NNH) had the highest Gibbs free energy barrier of 1.13 eV, which was the potential-determining step (PDS) of the whole process. The subsequent hydrogenation steps had

two pathways: one was the distal pathway, which involved continuous hydrogenation on the same N atom ($^*NNH \rightarrow ^*NNH_2$); another approach was the alternating pathway, where hydrogen protons reacted with two N atoms separately ($^*NNH \rightarrow ^*NNH$). The results indicated that hydrogenation through distal pathway had a larger upward energy barrier ($\Delta G=0.57$ eV), while hydrogenation through alternative pathways had a smaller upward energy barrier ($\Delta G=0.14$ eV). Since when both were endothermic reactions, the smaller the change in free energy, the greater the likelihood of the reaction occurring, Bi_2S_3/MoS_2 composites preferred to convert N_2 to NH_3 through alternating pathways. However, in the subsequent alternating hydrogenation reaction, the formation of $^*NNH \rightarrow ^*NNH_2$ and $^*NNH_2 \rightarrow ^*NH_2NH_2$ intermediates were both exothermic processes, and the free energy changed by -0.70 eV and -0.10 eV, respectively. During the subsequent hydrogenation process, on the one hand, due to the spontaneous exothermic reaction of $^*NH_2NH_2 \rightarrow ^*NH_2$, the free energy changed by -2.12 eV; on the other hand, the bridging adsorption of N_2 on the two Bi atoms also promoted the breaking of N-N bond, so no N_2H_4 byproducts were produced during the NRR process, which was in accordance with the experimental results. Therefore, the whole N_2 hydrogenation went through the process of $^*NN \rightarrow ^*NNH \rightarrow ^*NNH \rightarrow ^*NNH \rightarrow ^*NH_2NH_2 \rightarrow ^*NH_2 \rightarrow ^*NH_3$, and finally the desorption of NH_3 was completed. The calculated Gibbs free energy (ΔG) of all steps catalyzed by Bi_2S_3/MoS_2 composites were displayed in Table S2. Based on the above results, it could be certified that the constructed Bi_2S_3/MoS_2 composites could more firmly adsorb N_2 and activated it. The increase of NRR activity could be attributed to the introduction of Bi leading to the weakening of the adsorption of H^+ and inhibiting the occurrence of HER.

4. Conclusions

In summary, Bi_2S_3/MoS_2 composites had been prepared by a simple one-step hydrothermal method. The introduction of P-block element Bi promoted the adsorption and activation of N_2 , while 1 T- MoS_2 provided better electrical conductivity, which synergically improved the NRR performance. In 0.1 M Na_2SO_4 solution, Bi_2S_3/MoS_2 composites (BMS-5) demonstrated excellent NRR performance with an ammonia yield rate of $54.64 \mu g h^{-1} mg_{cat}^{-1}$ at -0.60 V vs. RHE, Faradic efficiency of 58.56 % at -0.40 V vs. RHE, and also exhibited good stability in 6 cycles and 12 hours of long-term electrolysis testing. The blank control experiment verified that the NH_3 synthesized originated from the incoming N_2 , and no by-product N_2H_4 was generated during the whole experiment, indicating that BMS-5 had outstanding selectivity. The theoretical calculation results showed that the whole N_2 hydrogenation process complied with an alternate pathway, and the first hydrogenation step was the potential determination step of the reaction. In addition, the results of in situ infrared spectroscopy measurements further confirmed the reliability of N_2 reduction for ammonia synthesis. This work contributes certain direction for the efficient nitrogen fixation reaction of P-block elements coupled transition metal electrocatalysts under environmental conditions.

CRediT authorship contribution statement

Yaru Wang: Investigation. **Guangmin Ren:** Writing – original draft, Investigation. **Xiaoyue Chen:** Writing – review & editing, Writing – original draft, Investigation. **Xiangchao Meng:** Writing – review & editing, Supervision, Investigation. **Zisheng Zhang:** Writing – review & editing, Supervision. **Zizhen Li:** Investigation.

Declaration of Competing Interest

The authors declare that they have no known competing financial interests or personal relationships that could have appeared to influence the work reported in this paper.

Data Availability

Data will be made available on request.

Acknowledgements

X.M. acknowledges the financial supports from National Natural Science Foundation of China (Grant No: 22002146) and Taishan Scholars Foundation of Shandong province (No.: tsqn201909058). The authors would like to thank e-Testing Service Platform (<https://www.eceshi.com>) for the XRD, XPS etc. analysis.

Appendix A. Supporting information

Supplementary data associated with this article can be found in the online version at [doi:10.1016/j.apcatb.2024.124173](https://doi.org/10.1016/j.apcatb.2024.124173).

References

- [1] H. Tabassum, S. Mukherjee, J. Chen, D. Holiharimanana, S. Karakalos, X. Yang, S. Hwang, T. Zhang, B. Lu, M. Chen, Z. Tang, E.A. Kyriakidou, Q. Ge, G. Wu, Hydrogen generation via ammonia decomposition on highly efficient and stable Ru-free catalysts: approaching complete conversion at 450 °C, *Energ. Environ. Sci.* 15 (2022) 4190–4200, <https://doi.org/10.1039/d1ee03730g>.
- [2] Y. Li, H.S. Pillai, T. Wang, S. Hwang, Y. Zhao, Z. Qiao, Q. Mu, S. Karakalos, M. Chen, J. Yang, D. Su, H. Xin, Y. Yan, G. Wu, High-performance ammonia oxidation catalysts for anion-exchange membrane direct ammonia fuel cells, *Energ. Environ. Sci.* 14 (2021) 1449–1460, <https://doi.org/10.1039/d0ee03351k>.
- [3] H. Zhu, X. Ren, X. Yang, X. Liang, A. Liu, G. Wu, Fe-based catalysts for nitrogen reduction toward ammonia electrosynthesis under ambient conditions, *SusMat* 2 (2022) 214–242, <https://doi.org/10.1002/sus2.70>.
- [4] Z. Li, M. Li, J. Yang, M. Liao, G. Song, J. Cao, F. Liu, Z. Wang, S. Kawi, Q. Lin, Electrocatalyst design strategies for ammonia production via N_2 reduction, *Catal. Today* 388–389 (2022) 12–25, <https://doi.org/10.1016/j.cattod.2021.06.008>.
- [5] S. Chatterjee, R.K. Parsapur, K.-W. Huang, Limitations of ammonia as a hydrogen energy carrier for the transportation sector, *ACS Energy Lett.* 6 (2021) 4390–4394, <https://doi.org/10.1021/acsenergylett.1c02189>.
- [6] Z. Zhao, G. Ren, Z. Zhang, X. Meng, Z. Li, Rapid Joule heating synthesis of Pt clusters on C_3N_4 with abundant nitrogen vacancies for highly-efficiently photocatalytic H_2 production, *Sep. Purif. Technol.* 330 (2024) 125393, <https://doi.org/10.1016/j.seppur.2023.125393>.
- [7] K. Chu, Y.-p Liu, Y.-b Li, Y.-l Guo, Y. Tian, Two-dimensional (2D)/2D Interface engineering of a MoS_2/C_3N_4 heterostructure for promoted electrocatalytic nitrogen fixation, *ACS Appl. Mater. Interfaces* 12 (2020) 7081–7090, <https://doi.org/10.1021/acsami.9b18263>.
- [8] C. Deng, C. Qi, X. Wu, G. Jing, H. Zhao, Unveiling the relationship between structural evaluation and catalytic performance of $InOOH$ during electroreduction of CO_2 to formate, *Green Carbon* (2024), <https://doi.org/10.1016/j.greenera.2024.02.003>.
- [9] M. Capdevila-Cortada, Electrifying the Haber–Bosch, *Nat. Catal.* 2 (2019) 1055–10515, <https://doi.org/10.1038/s41929-019-0414-4>.
- [10] H.-P. Jia, E.A. Quadrelli, Mechanistic aspects of dinitrogen cleavage and hydrogenation to produce ammonia in catalysis and organometallic chemistry: relevance of metal hydride bonds and dihydrogen, *Chem. Soc. Rev.* 43 (2014) 547–564, <https://doi.org/10.1039/c3cs60206k>.
- [11] J. Deng, J.A. Iniguez, C. Liu, Electrocatalytic nitrogen reduction at low temperature, *Joule* 2 (2018) 846–856, <https://doi.org/10.1016/j.joule.2018.04.014>.
- [12] Z. Zhao, G. Ren, Z. Zhang, X. Meng, Z. Li, Rapid Joule heating synthesis of Ni doped into porous honeycomb C_3N_4 with greatly improved photocatalytic H_2 production, *Inorg. Chem. Front.* (2024), <https://doi.org/10.1039/d4qi00225c>.
- [13] G. Lin, Q. Ju, X. Guo, W. Zhao, S. Adimi, J. Ye, Q. Bi, J. Wang, M. Yang, F. Huang, Intrinsic electron localization of metastable MoS_2 boosts electrocatalytic nitrogen reduction to ammonia, *Adv. Mater.* 33 (2021) 2007509, <https://doi.org/10.1002/adma.202007509>.
- [14] Y. Liu, M. Han, Q. Xiong, S. Zhang, C. Zhao, W. Gong, G. Wang, H. Zhang, H. Zhao, Dramatically enhanced ambient ammonia electrosynthesis performance by in-operando created Li–S interactions on MoS_2 electrocatalyst, *Adv. Energy Mater.* 9 (2019) 1803935, <https://doi.org/10.1002/aenm.201803935>.
- [15] J. Zhang, X. Tian, M. Liu, H. Guo, J. Zhou, Q. Fang, Z. Liu, Q. Wu, J. Lou, Cobalt-modulated molybdenum–dinitrogen interaction in MoS_2 for catalyzing ammonia synthesis, *J. Am. Chem. Soc.* 141 (2019) 19269–19275, <https://doi.org/10.1021/jacs.9b02501>.
- [16] R. Liu, H. Fei, J. Wang, T. Guo, F. Liu, J. Wang, Z. Wu, D. Wang, Insights of active sites separation mechanism for highly efficient electrocatalytic N_2 reduction to ammonia over glucose-induced metallic MoS_2 , *Appl. Catal. B Environ.* 337 (2023) 122997, <https://doi.org/10.1016/j.apcatb.2023.122997>.
- [17] Y. Sun, F. Alimohammadi, D. Zhang, G. Guo, Enabling colloidal synthesis of edge-oriented MoS_2 with expanded interlayer spacing for enhanced HER catalysis, *Nano Lett.* 17 (2017) 1963–1969, <https://doi.org/10.1021/acs.nanolett.6b05346>.

[18] R. Liu, H. Fei, J. Wang, T. Guo, F. Liu, Z. Wu, D. Wang, Unveiling the synergistic effect between the metallic phase and bridging S species over MoS₂ for highly efficient nitrogen fixation, *Appl. Catal. B Environ.* 343 (2024) 123469, <https://doi.org/10.1016/j.apcatb.2023.123469>.

[19] X. Chen, Y. Wang, X. Meng, Fabrication of NiS_x/MoS₂ interface for accelerated charge transfer with greatly improved electrocatalytic activity in nitrogen reduction to produce ammonia, *Chem. Eng. J.* 479 (2024) 147701, <https://doi.org/10.1016/j.cej.2023.147701>.

[20] X. Xu, B. Sun, Z. Liang, H. Cui, J. Tian, High-performance electrocatalytic conversion of N₂ to NH₃ using 1T-MoS₂ anchored on Ti₃C₂ MXene under ambient conditions, *ACS Appl. Mater. Interfaces* 12 (2020) 26060–26067, <https://doi.org/10.1021/acsmi.0c06744>.

[21] R. Li, J. Liang, T. Li, L. Yue, Q. Liu, Y. Luo, M.S. Hamdy, Y. Sun, X. Sun, Recent advances in MoS₂-based materials for electrocatalysis, *Chem. Commun.* 58 (2022) 2259–2278, <https://doi.org/10.1039/dlcc04004a>.

[22] S. Li, Y. Wang, Y. Du, X.D. Zhu, J. Gao, Y.C. Zhang, G. Wu, P-Block metal-based electrocatalysts for nitrogen reduction to ammonia: a mini review, *Small* 19 (2023) 2206776, <https://doi.org/10.1002/smll.202206776>.

[23] C. Lv, L. Zhong, Y. Yao, D. Liu, Y. Kong, X. Jin, Z. Fang, W. Xu, C. Yan, K.N. Dinh, M. Shao, L. Song, G. Chen, S. Li, Q. Yan, G. Yu, Boosting electrocatalytic ammonia production through mimicking “π back-donation”, *Chem* 6 (2020) 2690–2702, <https://doi.org/10.1016/j.chempr.2020.07.006>.

[24] Y. Sun, Y. Wang, H. Li, W. Zhang, X.-M. Song, D.-M. Feng, X. Sun, B. Jia, H. Mao, T. Ma, Main group metal elements for ambient-condition electrochemical nitrogen reduction, *J. Energy Chem.* 62 (2021) 51–70, <https://doi.org/10.1016/j.jecchem.2021.03.001>.

[25] L. Li, C. Tang, B. Xia, H. Jin, Y. Zheng, S.-Z. Qiao, Two-dimensional Mosaic bismuth nanosheets for highly selective ambient electrocatalytic nitrogen reduction, *ACS Catal.* 9 (2019) 2902–2908, <https://doi.org/10.1021/acscatal.9b00366>.

[26] Y. Luo, P. Shen, X. Li, Y. Guo, K. Chu, Sulfur-deficient Bi₂S_{3-x} synergistically coupling Ti₃C₂T_x-MXene for boosting electrocatalytic N₂ reduction, *Nano Res.* 15 (2022) 3991–3999, <https://doi.org/10.1007/s12274-022-4097-9>.

[27] Y.-C. Hao, Y. Guo, L.-W. Chen, M. Shu, X.-Y. Wang, T.-A. Bu, W.-Y. Gao, N. Zhang, X. Su, X. Feng, J.-W. Zhou, B. Wang, C.-W. Hu, A.-X. Yin, R. Si, Y.-W. Zhang, C.-H. Yan, Promoting nitrogen electroreduction to ammonia with bismuth nanocrystals and potassium cations in water, *Nat. Catal.* 2 (2019) 448–456, <https://doi.org/10.1038/s41929-019-0241-7>.

[28] C. Lv, J. Liu, C. Lee, Q. Zhu, J. Xu, H. Pan, C. Xue, Q. Yan, Emerging p-Block-element-based electrocatalysts for sustainable nitrogen conversion, *ACS Nano* 16 (2022) 15512–15527, <https://doi.org/10.1021/acsnano.2c07260>.

[29] X. Li, T. Li, Y. Ma, Q. Wei, W. Qiu, H. Guo, X. Shi, P. Zhang, A.M. Asiri, L. Chen, B. Tang, X. Sun, Boosted electrocatalytic N₂ reduction to NH₃ by defect-rich MoS₂ nanoflower, *Adv. Energy Mater.* 8 (2018) 1801357, <https://doi.org/10.1002/aenm.201801357>.

[30] M.S. Islam, M. Kim, X. Jin, S.M. Oh, N.-S. Lee, H. Kim, S.-J. Hwang, Bifunctional 2D superlattice electrocatalysts of layered double hydroxide-transition metal Dichalcogenide active for overall water splitting, *ACS Energy Lett.* 3 (2018) 952–960, <https://doi.org/10.1021/acsenergylett.8b00134>.

[31] N. Gao, H. Yang, D. Dong, D. Dou, Y. Liu, W. Zhou, F. Gao, C. Nan, Z. Liang, D. Yang, Bi₂S₃ quantum dots in situ grown on MoS₂ nanoflowers: an efficient electron-rich interface for photoelectrochemical N₂ reduction, *J. Colloid Interface Sci.* 611 (2022) 294–305, <https://doi.org/10.1016/j.jcis.2021.12.096>.

[32] W. Ye, M. Arif, X. Fang, M.A. Mushtaq, X. Chen, D. Yan, Efficient photoelectrochemical route for the ambient reduction of N₂ to NH₃ based on nanojunctions assembled from MoS₂ nanosheets and TiO₂, *ACS Appl. Mater. Interfaces* 11 (2019) 28809–28817, <https://doi.org/10.1021/acsmi.9b06596>.

[33] L. Fang, Y. Qiu, T. Zhai, F. Wang, M. Lan, K. Huang, Q. Jing, Flower-like nanoarchitecture assembled from Bi₂S₃ nanorod/MoS₂ nanosheet heterostructures for high-performance supercapacitor electrodes, *Colloids Surf. A Physicochem. Eng. Asp.* 535 (2017) 41–48, <https://doi.org/10.1016/j.colsurfa.2017.09.022>.

[34] L. Zhou, T. Yang, S. Chen, J. Gao, X. Wang, P. He, H. Lei, D. Yang, F. Dong, L. Jia, B. Jia, H. Zhang, Tunably fabricated nanotremella-like Bi₂S₃/MoS₂: an excellent and highly stable electrocatalyst for alkaline hydrogen evolution reaction, *Int. J. Hydron. Energy* 45 (2020) 9535–9545, <https://doi.org/10.1016/j.ijhydene.2020.01.168>.

[35] X. Liu, X. Xu, F. Li, J. Xu, H. Ma, X. Sun, D. Wu, C. Zhang, X. Ren, Q. Wei, Heterostructured Bi₂S₃/MoS₂ nanoarrays for efficient electrocatalytic nitrate reduction to ammonia under ambient conditions, *ACS Appl. Mater. Interfaces* 14 (2022) 38835–38843, <https://doi.org/10.1021/acsmi.2c10323>.

[36] F. Chen, Y. Cao, D. Jia, Facile synthesis of Bi₂S₃ hierarchical nanostructure with enhanced photocatalytic activity, *J. Colloid Interface Sci.* 404 (2013) 110–116, <https://doi.org/10.1016/j.jcis.2013.04.013>.

[37] X. Chen, S. Zhang, X. Qian, Z. Liang, Y. Xue, X. Zhang, J. Tian, Y. Han, M. Shao, Enabling efficient electrocatalytic conversion of N₂ to NH₃ by Ti₃C₂ MXene loaded with semi-metallic 1T'-MoS₂ nanosheets, *Appl. Catal. B Environ.* 310 (2022) 121277, <https://doi.org/10.1016/j.apcatb.2022.121277>.

[38] M. Li, J. Wang, P. Zhang, Q. Deng, J. Zhang, K. Jiang, Z. Hu, J. Chu, Superior adsorption and photoinduced carries transfer behaviors of dandelion-shaped Bi₂S₃@MoS₂: experiments and theory, *Sci. Rep.* 7 (2017) 42484, <https://doi.org/10.1038/srep42484>.

[39] D. Han, N. Gao, J. Ge, C. Liu, W. Xing, Activating MoS₂ via electronic structure modulation and phase engineering for hydrogen evolution reaction, *Catal. Commun.* 164 (2022) 106427, <https://doi.org/10.1016/j.catcom.2022.106427>.

[40] S. Ali Shah, L. Xu, R. Sayyar, T. Bian, Z. Liu, A. Yuan, X. Shen, I. Khan, A. Ali Tahir, H. Ullah, Growth of MoS₂ nanosheets on M@N-doped carbon particles (M = Co, Fe or CoFe Alloy) as an efficient electrocatalyst toward hydrogen evolution reaction, *Chem. Eng. J.* 428 (2022) 132126, <https://doi.org/10.1016/j.cej.2021.132126>.

[41] D. Wang, X. Zhang, S. Bao, Z. Zhang, H. Fei, Z. Wu, Phase engineering of a multiphasic 1T/2H MoS₂ catalyst for highly efficient hydrogen evolution, *J. Mater. Chem. A* 5 (2017) 2681–2688, <https://doi.org/10.1039/c6ta09409k>.

[42] W. Wu, X. Ren, C. Zhang, Y. Ding, H. Gai, M. Xiao, Q. Zhu, H. Song, T. Huang, Targeted fabrication of 1T-MoS₂ enriched nanosheets vertically oriented on spiny-shaped nanospheres with sufficient sulfur vacancies and “rim” sites for co-enhancing the hydrodesulfurization activity and hydrogenation selectivity, *J. Catal.* 428 (2023) 115195, <https://doi.org/10.1016/j.jcat.2023.115195>.

[43] X. Chen, S. Lu, Y. Wei, M. Sun, X. Wang, M. Ma, J. Tian, Basal plane-activated boron-doped MoS₂ nanosheets for efficient electrochemical ammonia synthesis, *ChemSusChem* (2022) e202202265, <https://doi.org/10.1002/cssc.202202265>.

[44] X. Chen, C. Ma, Z. Tan, X. Wang, X. Qian, X. Zhang, J. Tian, S. Yan, M. Shao, One-dimensional screw-like MoS₂ with oxygen partially replacing sulfur as an electrocatalyst for the N₂ reduction reaction, *Chem. Eng. J.* 433 (2022) 134504, <https://doi.org/10.1016/j.cej.2022.134504>.

[45] M. Xie, F. Dai, H. Guo, P. Du, X. Xu, J. Liu, Z. Zhang, X. Lu, Improving electrocatalytic nitrogen reduction selectivity and yield by suppressing hydrogen evolution reaction via electronic metal-support interaction, *Adv. Energy Mater.* 13 (2023) 2203032, <https://doi.org/10.1002/aenm.202203032>.

[46] P. Li, Z. Zhou, Q. Wang, M. Guo, S. Chen, J. Low, R. Long, W. Liu, P. Ding, Y. Wu, Y. Xiong, Visible-light-driven nitrogen fixation catalyzed by Bi₂O₃Br Nanostructures: enhanced performance by oxygen vacancies, *J. Am. Chem. Soc.* 142 (2020) 12430–12439, <https://doi.org/10.1021/jacs.0c05097>.

[47] Y. Zhang, L. Ran, Y. Zhang, P. Zhai, Y. Wu, J. Gao, Z. Li, B. Zhang, C. Wang, Z. Fan, X. Zhang, J. Cao, D. Jin, L. Sun, J. Hou, Two-dimensional defective boron-doped niobic acid nanosheets for robust nitrogen photofixation, *ACS Nano* 15 (2021) 17820–17830, <https://doi.org/10.1021/acsnano.1c06017>.

[48] Z. Zhang, N. Lu, W. Cai, J. Wen, K. Li, H. Qu, A novel Zn-doped CHA zeolite coupled CDS for photocatalytic nitrogen fixation, *Mol. Catal.* 549 (2023) 113471, <https://doi.org/10.1016/j.mcat.2023.113471>.

[49] Y. Wang, Y. Zhang, Y. Gao, D. Wang, Modulating Lewis acidic active sites of Fe doped Bi₂MoO₆ nanosheets for enhanced electrochemical nitrogen fixation, *J. Colloid Interface Sci.* 646 (2023) 176–184, <https://doi.org/10.1016/j.jcis.2023.05.012>.

[50] M. Yuan, J. Chen, Y. Bai, Z. Liu, J. Zhang, T. Zhao, Q. Wang, S. Li, H. He, G. Zhang, Unveiling electrochemical urea synthesis by Co-activation of CO₂ and N₂ with Mott–Schottky heterostructure catalysts, *Angew. Chem. Int. Ed.* 60 (2021) 10910–10918, <https://doi.org/10.1002/anie.202101275>.